RESEARCH ARTICLE

Perovskite modules with 99 % geometrical fill factor using point contact interconnections design

Lucija Rakocevic[1,2] | **Gunnar Schöpe**[3] | **Bugra Turan**[3] | **Jan Genoe**[1,2] | **Tom Aernouts**[1] | **Stefan Haas**[3] | **Robert Gehlhaar**[1] | **Jef Poortmans**[1,2,4]

[1]imec - partner in EnergyVille and Solliance, Leuven, 3001, Belgium

[2]Departement Elektrotechniek - ESAT , Katholieke Universiteit Leuven, Leuven, 3001, Belgium

[3]IEK5 – Photovoltaik, Forschungszentrum Jülich GmbH, Jülich, 52425, Germany

[4]Physics, University of Hasselt, Diepenbeek, 3590, Belgium

Correspondence
Lucija Rakocevic, imec, Leuven, 3001, Belgium
Email: lucija.rakocevic@gmail.com

Funding information
European Union, H2020 Program, Grant Number: 764047; Interreg V program Flanders-Netherlands, PVopMaat project; Kuwait Foundation for the Advancement of Sciences under project number CN18-15EE-01

Thin film photovoltaic technology, based on hybrid metal halide perovskites, has achieved 25.2 % and 16.1 % certified power conversion efficiencies for solar cell and solar module devices, respectively. Still, the gap between power conversion efficiency of small area solar cells and large area solar modules is greater than for any other photovoltaic technology. Analysis of loss mechanisms in n-i-p solution processed devices defined layer inhomogeneity loss and inactive area loss as the two most prominent loss mechanisms in upscaling. In this study we focus on minimizing inactive area loss. We analyze the point contact interconnections design and demonstrate it on perovskite thin film solar modules to achieve a geometrical fill factor of up to 99 %. Numerical and analytical simulations are utilized to optimize interconnections and solar module design and balance inactive area loss, series resistance loss and contact resistance loss.

KEYWORDS
perovskite thin-film modules, upscaling losses, geometrical fill factor, point contact, interconnections

1 | INTRODUCTION

Hybrid metal halide perovskite based thin-film photovoltaic technology proved its ability to achieve power conversion efficiencies (PCE) higher than any other single junction thin-film photovoltaic technology. The highest certified PCE for a perovskite solar cell is 25.2 % for a device area of 0.1 cm^2 [1, 2, 3], while for a perovskite solar module it is 16.1 % for an aperture area of 802 cm^2 [4]. Even though these are impressive results for perovskite thin film photovoltaic technology, there is still an upscaling loss of at least 35 % between best certified small area solar cells and best large area solar modules (Figure 1a). Based on latest results, the upscaling loss is decreasing. The small area solar cell to large area solar module upscaling loss consists of four interdependent loss mechanisms: layer inhomogeneity loss, P2 ohmic loss, sheet resistance loss and inactive area loss [5]. Increase in the knowledge of interface engineering, perovskite crystallization dynamics and solution engineering adapted to upscalable deposition methods lead to devices with improved layer homogeneity and PCE [5, 6, 7, 8, 9, 10]. Intensified research efforts on the upscaling of perovskite solar modules using other deposition methods, such as evaporation have yielded improved performances as well [11, 12].

Other three interdependent losses, namely, P2 ohmic loss, sheet resistance loss and inactive area loss can be minimized with optimal interconnections patterning [13] and solar module design. This study focuses on minimizing inactive area loss by changing the interconnections design from classical line contact to point contact for solar modules with monolithic serially interconnected cells (Figure 2). In order to achieve a decrease in inactive area loss while keeping P2 ohmic loss and sheet resistance loss low, solar module design should be optimized too.

Inactive area loss is a geometrical loss calculated as ratio of the inactive area to solar module aperture area. Inactive area is the area between P1 and P3 interconnections. The solar cells are serially connected through the ohmic P2 interconnection. P1 and P3 interconnections need to assure isolation of either the front or the back electrode, respectively.

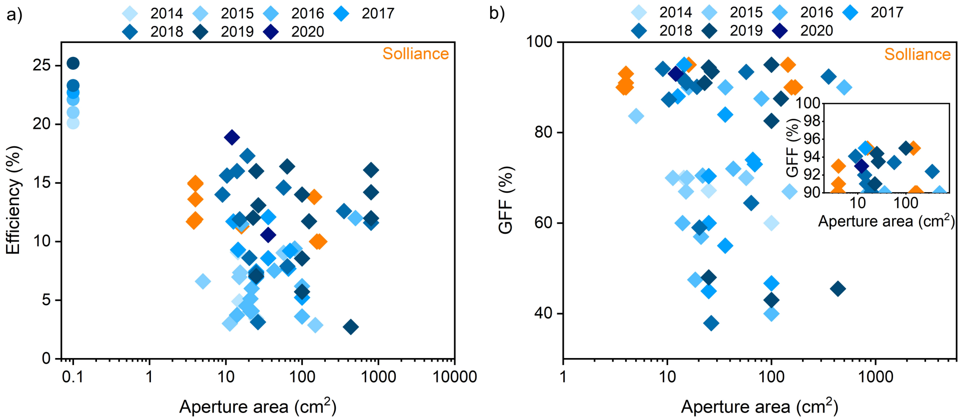

FIGURE 1 Overview of published perovskite solar module aperture area versus a) power conversion efficiencies and b) GFF [4, 10, 12, 14, 15]. Circular data points in a) represent highest certified small area solar cell for a specific year [1].

The measure used to define the ratio of the active area to the aperture area of the solar module is the geometrical fill factor (GFF). Figure 1b shows reported GFF for published perovskite modules to date [4, 10, 12, 14, 15]. The highest GFF achieved is 95 % [9, 16] using ps pulsed laser patterning. Hence, the module inactive area loss is 5 % or more, making this the second most significant loss mechanism after layer inhomogeneity loss [5]. In this work we show how an inactive area loss can be decreased from 5 to 1 % by optimizing the design of the module to point contact interconnections [17] and processing perovskite modules with 98.5 and 99 % GFF.

2 | EXPERIMENTAL DETAILS

Devices used in this study are the planar n-i-p perovskite solar modules processed on 0.7 mm thick glass substrates with the area of 3 by 3 cm^2. Processing is performed in the N_2 atmosphere, unless otherwise specified. Glass substrates with 150 nm indium tin oxide (ITO) layer (10 - 25 Ω/□) are acquired from Colorado Concept Coatings LLC. P1 laser patterning is completed before cleaning. Solar module aperture area is 4 cm^2 (2 by 2 cm^2), with 4 serially connected cells of 5 mm length. Samples are cleaned using successive steps in soap/distilled water/acetone/isopropyl alcohol (IPA) at 55 °C in ultrasonic bath.

A layer of 20 nm of compact titanium oxide, serving as the electron transport layer, is deposited using electron beam evaporation [18]. The perovskite active layer is $CH_3NH_3PbI_{3-x}Cl_x$ (MAPI). It is formed from the precursor solution that consists of mixed lead source of $Pb(CH_3CO_2)_2 \cdot 3H_2O$ with 20 % $PbCl_2$ and CH_3NH_3I using dimethylformamide (DMF) as a solvent [19]. The layer is processed using one-step spin coating followed by a 10 minute thermal annealing at 130 °C. Hole transport layer is formed using spin coating of 2,2', 7,7'- tetrakis (N,N-di-p-methoxyphenylamine) 9,9'-spirobifluorene (Spiro-OMeTAD) dissolved in chlorobenzene (80 mg/mL) doped with 28.5 μL/mL of 4-tert-butylpyridine and 17.5 μL/mL of bis(trifluoromethane)sulfonimide lithium salt (Li-TFSI, 520 mg/mL in acetonitrile). Prior to the back contact deposition, the devices are placed in a dry air box for 12 hours of oxygen doping of the 250 nm thick, amorphous Spiro-OMeTAD layer. Laser patterning is used to remove the transport layers and photoactive layer and expose ITO electrode for the P2 interconnection (Fig 2). Back electrode is a thermally evaporated 80 nm thick gold layer. To complete solar module processing, laser or mechanical patterning [13] is used for P3 interconnection. Therefore the final device stack consists of the glass/ITO/TiO_2/$CH_3NH_3PbI_{3-x}Cl_x$/doped Spiro-OMeTAD/Au.

For patterning we used ns and ps laser systems or mechanical patterning. Rofin RSY20E THG 355 nm ns pulsed Nd:YVO4 q-switched laser was used for the P2 point contact interconnection (7 ns laser pulse, 15 kHz frequency and 191 mW average power, ablated from the glass side) and the P3 interconnection (7 ns laser pulse, 15 kHz frequency and 10 mW average power, ablated from the film side). MSV 500 ps pulsed laser system integrated in the nitrogen glovebox has been used with 355 nm wavelength for classical P1, P2 and P3 (10 ps laser pulse, 200 kHz frequency and 360, 86 and 74 mW average power, respectively, ablated from the film side) patterning. Mechanical patterning used for the P2 and P3 interconnections of the reference modules has been explained in detail in a previous study [13].

The devices were illuminated with an AM1.5G spectrum generated by a class A solar simulator (Abet Sun 2000). Hysteresis current-voltage measurements are performed by stepping through applied voltage in reverse (V_{OC} to J_{SC}) and forward (J_{SC} to V_{OC}) direction with a scan speed of 1.0 or 4.9 V/s for solar cells or modules respectively. Maximum power point tracking performance is measured for 180 seconds using a tracking algorithm [20] with measurement delay of 3 seconds and voltage step of 10 to 50 mV.

3 | RESULTS AND DISCUSSION

Prior to the demonstration of perovskite solar modules with point contact interconnections, we will discuss the point contact interconnections design and its effects on module design and losses. The difference between classical line

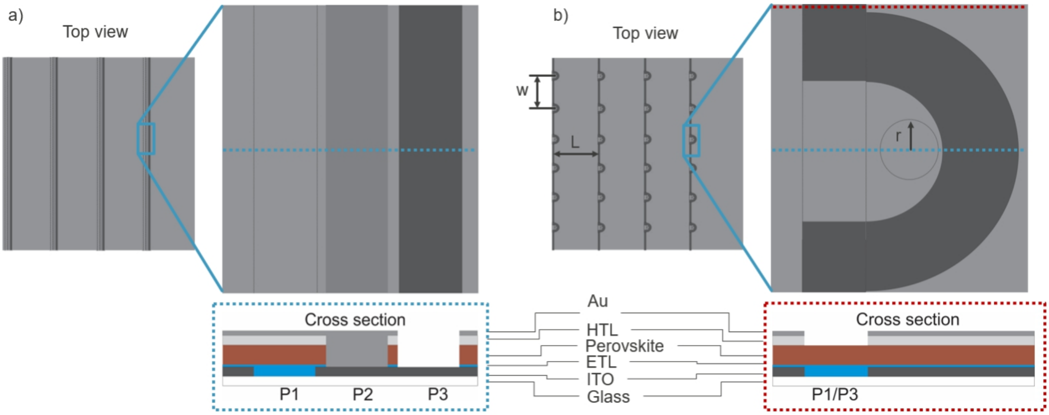

FIGURE 2 Top view and cross section of a solar module with 4 cells connected in series with a magnified view of a) classical and b) point contact interconnections. Blue and red dotted lines indicate where the cross-sections are taken. The red dotted cross-section represents the part of the point contact interconnection where P1 and P3 interconnections overlap.

contact and point contact interconnection design is seen from the top view of the modules, shown in schemes in Figure 2 [17]. The point contact interconnections design utilizes low P2 contact resistivity between the front and the back electrode in order to decrease the contact area in P2 interconnection. The P2 contact area changes from a rectangular area with line contact to multiple circular areas with the point contact design. Discontinuity in the P2 interconnection allows for the P3 interconnection line to meander around P2 points and to predominantly overlap with the P1 interconnection, decreasing the inactive area of the cell (Figure 2b).

To take advantage of the point contact interconnection design, effects of this interconnection on the solar module design are analyzed. The point contact interconnection design has multiple parameters that can influence the solar module performance (Figure 2b) and they are as follows:

- P2 point contact, which includes both size (radius, *r*) and the shape (circular) of the contact;
- Distance between P2 points, *w*;
- Length of the cell in a modules, L_c;
- Width of P1 and P3 and the distance between P1-P2 and P2-P3 at the point contact area;
- Shape of the P3 interconnection around the P2 point.

Although a purpose of the point contact interconnection is to minimize the inactive area loss, its implementation will also affect the sheet resistance loss as well as the P2 electrical loss. Varying the size of the inactive area of the module requires re-optimization of the L_c in order to achieve minimal sheet resistance loss. P2 electrical loss depends on the contact resistance of the P2 which is affected by contact resistivity between ITO and Au at the P2 point contact, point contact geometry, *w* and L_c.

Parameters such as the P1 and P3 width as well as the distance between these interconnections are determined based on the laser system limitations and perovskite stack characteristics. In experiments presented here, they are constant. The shape of the P3 interconnection is rectangular (Figure 8a) and not circular, as demonstrated in Figure 2b. This parameter is not expected to have a significant effect on performance as it relates to the low-ohmic gold back electrode. Moreover, effects of the shape of both the P3 interconnection and the P2 point contact on the performance of thin film solar modules were analyzed in a theoretical study by Krumscheid et al. [21]. Assuming negligible contact resistivity at P2, it was concluded that the shape of the P2 contact (circle, square, triangle) or P3 (circular, rectangular, etc.) do not affect performance of the solar modules. Therefore, in this study the shape of the P2 contact remained circular.

In a subsequent analysis we demonstrate how the radius of the circular P2 point contact (*r*), the distance between points (*w*) and the length of the cell (L_c) can affect the interconnection losses and hence the performance of the solar module. To be able to quantify losses stemming from these changes, P2 contact resistivity of the ITO/Au contact formed using ns laser patterning was determined.

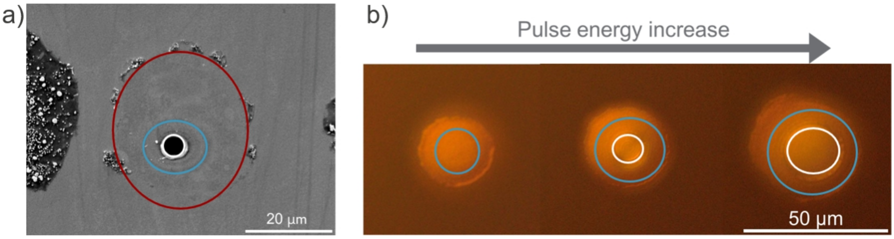

FIGURE 3 a) SEM image of one P2 point contact. Circles indicate laser ablation regions with affected TiO_2 (red), removed TiO_2 (blue) and removed ITO (white). b) Optical microscope images of P2 points imaged from glass side of the substrate with all the stack layers present. The circles indicate TiO_2 removal area where ITO is exposed to direct contact with Au (blue) and ITO removal area (white).

P2 contact resistivity

The goal of the P2 interconnection is to create a low resistance ohmic contact between the front (ITO) and the back electrode (Au). P2 is patterned before the deposition of the back contact. Therefore, laser ablation is used to remove Spiro-OMeTAD, MAPI perovskite and compact TiO_2 layers. The point ablation results in a circular removal of HTL and perovskite and partial removal of TiO_2, as indicated by the red circle in Figure 3a. For this SEM image, the back contact, HTL and perovskite have been chemically removed to leave glass/ITO/TiO_2 for inspection. As demonstrated in Figure 3a, the blue circle indicates an area with complete removal of TiO_2, while the white circle is the area where ITO is removed. Additionally, Figure 3b shows that with an increase in laser pulse energy, both the TiO_2 removal area (indicated by the blue circles) as well as the area of ITO removal (white circles) increase. Therefore, the contact between ITO/Au is the donut shaped area between the blue and white circles. As such, from the point forward we will treat it as a circular contact.

The first step to quantifying the P2 resistance loss is determining the contact resistivity of the formed contact using the transfer line method (TLM). Using TLM, contact resistivity can be calculated by varying the P2 contact length, *L* as shown in Figure 4a [13]. If the same approach is used for the point contact P2, the contact resistivity can be estimated utilizing the data and equation shown in Figure 4b. It should be noted that the P2 contact length is increased by increasing the number of points in the y-direction and with the assumption that the n points in that direction, the contact length is equal the sum of the n diameters (inset in Figure 4b). The P2 contact resistivity is determined to be 8×10^{-4} Ωcm^2. However, this approach assumes a linear current flow through a rectangular line contact of the front and the back electrode, which is not representative of the point contacts between ITO/Au.

Therefore, in order to determine the exact contact resistivity of the P2 point contact, the point TLM approach has been used, as indicated in Figure 5a [22, 17]. Using this design each measurement consists of measuring resistance

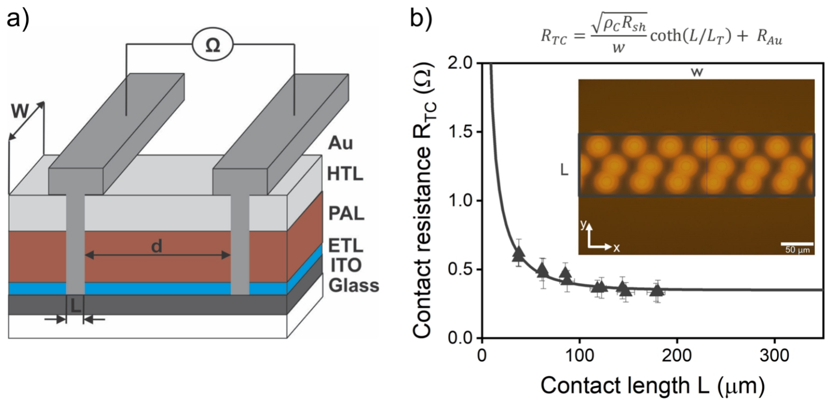

FIGURE 4 a) Schematic of the line contact TLM b) Changes in measured total contact resistance with an increase in contact length *L* for ns pulsed laser point contact P2. Fitting equation used to calculate contact resistivity ρ_c for the line contact is given above the graph [13]. Inset showing the optical microscope image of the point contact line, with *L* and *w*.

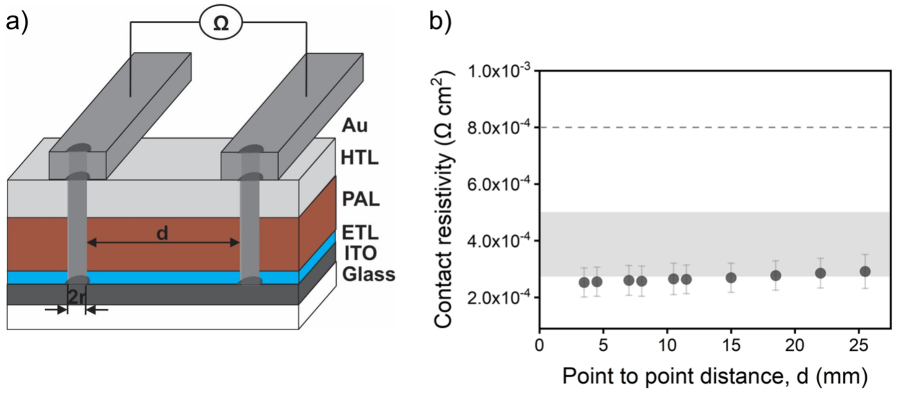

FIGURE 5 a) Schematic of the point contact TLM used for determining the P2 contact resistance and resistivity. b) Average contact resistivity of the point contact between ITO/Au, ρ_{point}, for six samples. Black dotted line represents the results shown in Figure 4b and the gray band is indicative of the results for the laser patterned line contact[13].

between two single 40 μm diameter point contacts located on large conductive pads of 12.5 mm^2 (2.5 by 5.0 mm^2). As can be seen from Figure 5a, the measured resistance between the two points is the sum of the resistance of Au strips, ITO strip in between the point contact and the point resistances (Equation 1). The contact resistivity of the ITO/Au contact at the point, for the case where small single point is located on large rectangular pad, can be determined directly from the R_{point} (Equation 2) [22].

$$R_T = 2R_{point} + 2R_{Au} + R_{ITO} \tag{1}$$

$$R_{point} \approx \frac{\rho_{point}}{\pi r^2} \tag{2}$$

In order to determine point's contact resistivity, ρ_{point} , six TLM samples were measured. The samples targeted identical geometry, wherein the resultant point contacts had ellipsoidal shape with the x-dimension of 40.8 ± 4.0 μm and the y-dimension of 48.1 ± 1.0 μm. Taking into account the area of the point contact, the ρ_{point} is determined to be up to 3×10^{-4} Ωcm^2 utilizing equations 1 and 2 (Figure 5b). In Figure 5b, the results are compared to the contact resistivity results from Figure 4b (dotted line) and the contact resistivity calculated for the laser patterned P2 line contact from a previous study [13] (gray band), in order to show that the presented P2 point contact has a comparably low contact resistivity. Sample to sample variation stems partially from the positioning of the point contact on the measurement pad. The difference in measured total resistance of up to 4 Ω and potential distribution of the different geometries have been modeled using SourceField [23].

Module and interconnection design

Knowing the P2 contact resistivity, we simulate point contact interconnected modules using Photovoltaic Module Simulator (PVMOS) [24], an open source ordinary differential equation solver.

First, we analyze the effect of varying the radius of the circular point contact on the module performance. Figure 6a shows how the variation in the P2 point contact radius and contact resistivity affect the module performance. Based on the graph, the point contact interconnection is optimal if the contact resistivity is lower than 10^{-3} Ωcm^2 and radius higher than 18 μm. For the presented results the GFF is assumed to be 98.5 %, the spot separation w=2 mm, the cell length L_c=5 mm and the interconnection geometry is defined based on the sample shown in Figure 8a (P1=50 μm, P3=30 μm). For comparison, analysis of the optimal P2 line contact has been demonstrated previously [13].

Further optimization of the module design is done by varying the distance between P2 points (w) and cell length (L_c). Width of P1 and P3 is assumed to be 100 μm with a radius of P2 of 40 μm. Sheet resistance of ITO and Au as front and back electrodes is 12 and 0.5 Ω/□. Diode parameters are set based on the cell measurements of the TiO_2/MAPI stack. Figure 6b shows the optimal module design in the red area of the graph.

With changes in the point to point distance, w, the size of the inactive area of the module varies. Therefore, cell length has to be optimized to assure optimal balance between contact resistance, inactive area and sheet resistance loss. The ideal point contact solar module design is shown in the Figure 6b as a black dot with the optimal point to point distance of 1.4 mm and cell length of 3.7 mm. However, for the purpose of this study, modules with cell length of 5 mm are used. Hence, the optimal point to point distance is 1.0 mm, as shown with the white square in the Figure 6b. Moreover to experimentally test the optimal point contact distance (w), solar modules with cell length of 5 mm and interconnection design as shown in Figure 7a are used. Due to the classical P3, these samples do not have the advantage of increase in active area expected from point contact interconnections. P2 point contact distance was

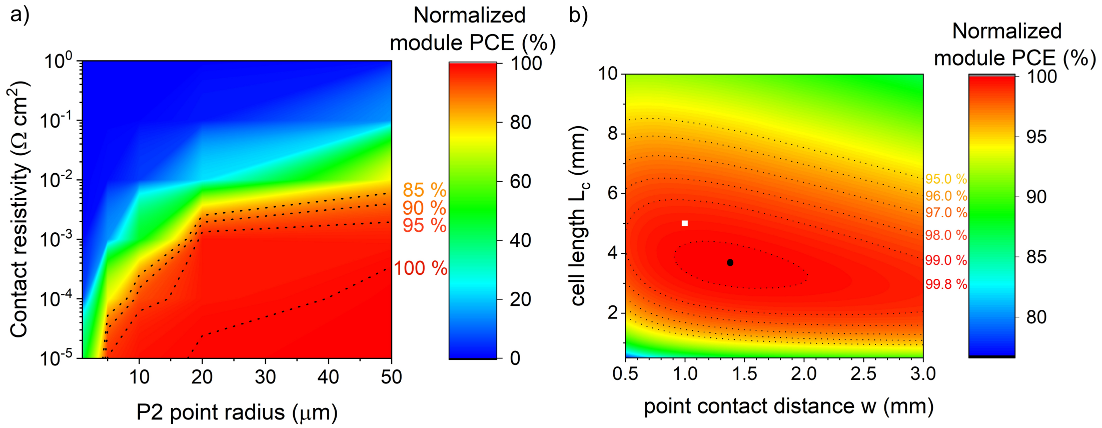

FIGURE 6 Results of PVMOS simulation. a) Map of normalized module efficiencies depending on the P2 contact resistivity and the P2 point contact radius. b) Map of normalized module efficiencies depending on the distance between points, w and length of the cell, L_c. L_c and w values for the optimal module with point contact interconnections (black circle) and optimal w for fixed L_c of 5 mm (white square). The highest efficiency represents the module with 13.1 % efficiency, which is 94.2 % of the champion 0.1 cm^2 cell.

varied from 53 μm to 3 mm (Figure 7b). Performance of the solar modules is comparable for devices with P2 point contact distance of up to 2 mm, while further increase in *w* leads to a decrease in solar module performance. The red line represents the decrease in PCE based on the simulation results from Figure 6b. The same trend is also visible with FF, but not with V_{OC} and J_{SC}. The variation in results of the samples is due to the sample-to-sample and batch-to-batch variations of spin coated solar modules, as discussed in our previous work [5].

Taking into account the experimental and simulation results, we conclude that the optimal P2 point contact distance for modules with 5 mm cell length is 2 mm. This P2 point contact distance allows for increase in GFF without compromising on performance. For fabrication of modules with point contact P1-P3 interconnections, modules with the P2 point contact distance (*w*) of 2 mm and 8 mm are processed. Point contact P2 and P3 are patterned using the UV ns pulsed laser. Their performance is compared to reference modules with line interconnections (Figure 2a) where P2 is patterned by the UV ns pulsed laser or by mechanical patterning. For reference modules P3 is patterned using mechanical patterning. Optical microscope images of the top view of the modules from the back contact side are shown in Figure 8a. Using such point contact design with the P2 point contact distance of 2 or 8 mm, modules with 98.5 or 99 % geometrical fill factor are achieved.

Resulting J-V curves and average efficiencies are demonstrated in Figure 8b. Due to point contact interconnections and very high geometrical fill factor, the point contact modules show higher J_{SC}. However, the decrease in V_{OC} and FF are not expected based on the simulation and experimental results from Figure 6 and Figure 7. Moreover, if decrease in performance was caused solely by increase in contact resistance, solar modules with P2 point distance, *w* of 2 mm would be better performing than modules with *w* of 8 mm, which is not the case. Simulation of point contact modules reveals that the measured decrease in performance is due to an increase in J_O, indicating additional recombination. The source of the additional recombination is assumed to be due to the thermal effects of the ns pulsed laser P3 patterning on the quality of the interfaces in perovskite stack, as well as on the perovskite material itself [25, 26, 27]. For the processing of the P3 interconnection, the shallow P3 has been used [25] in order to ensure a lower thermal effect of laser patterning. However, studied modules use a perovskite stack that faces problems due to TiO_2/MAPI

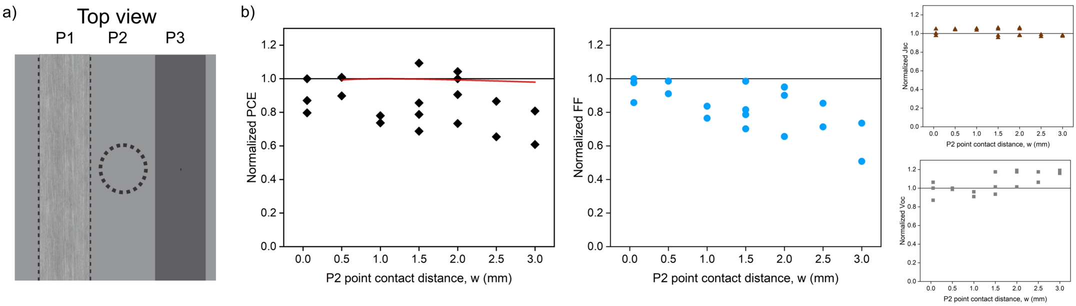

FIGURE 7 a) Top view scheme of the P2 point contact and P3 classical interconnection used for the test solar modules. b) PCE, FF, V_{OC} and J_{SC} of the resulting solar modules with cell length of 5 mm and varying *w* from 53 μm to 3 mm normalized to the modules with the lower w. Red line in the PCE graph represents the simulated decrease in PCE from Figure 6b.

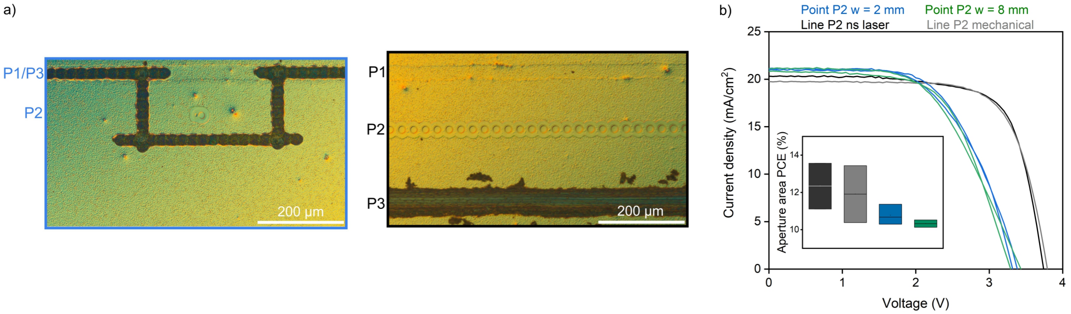

FIGURE 8 a) Optical microscope images of the top view of the interconnections of the fabricated modules with the point contact interconnection (left) and line contact (P2 ns laser and P3 mechanical) interconnection (right) from back electrode side. b) J-V curves of the champion modules showing hysteresis of TiO_2/MAPI stack. Inset are average efficiency of modules of each type.

interface [28, 29] and MAPI perovskite that has been shown to degrade and form PbI_2 due to laser induced thermal effects [26, 25]. Barbe et.al. [26] show that laser induced degradation causes an increase in the series resistance of the device, and thus hampering performance [26]. Finally, Spiro-OMeTAD degrades with temperature increase above 65 °C [30]. Therefore, it is expected that decrease in performance of point contact modules, visible in decrease in V_{OC} and FF is mainly due to thermal instability of the chosen perovskite stack and not inherent to the point contact interconnection design.

4 | CONCLUSION

The cell-to-module performance gap for the perovskite based thin-film photovoltaics is decreasing mainly due to improved layer homogeneities for larger area devices. The monolithic module devices experience losses due to the design that includes sheet resistance loss, P2 electrical loss and inactive area loss ultimately accounting for a loss of at least 6 $\%_{rel.}$. With maximum reported geometrical fill factor for the perovskite modules of 95 %, inactive area loss is the most significant. The current study shows how replacing the line interconnections design with the point contact design can help decrease these losses from 5 to 1 %. Moreover, laser patterned point contact is electrically characterized to determine contact resistivity. Finally, perovskite solar module simulations are utilized to determine optimal point contact size and interconnection and solar module design that would result in highest module performance. As a result we present perovskite modules with geometrical fill factors of up to 99 %. Further work is focused on using point contact design with thermally stable perovskite architectures and analysis of the effect of ns and ps laser patterning on structural and chemical properties of the devices.

Acknowledgements

This work is has been funded partly from the European Union's H2020 Programme for research, technological development and demonstration under grant agreement no. 764047 of the ESPResSo project, in part by European Regional Development Fund through the PVopMaat project within the Interreg V program Flanders-Netherlands and in part by the Kuwait Foundation for the Advancement of Sciences under project number CN18-15EE-01.

references

[1] Best Research-Cell Efficiency Chart | Photovoltaic Research | NREL;. `https://www.nrel.gov/pv/cell-efficiency.html`.

[2] Jung EH, Jeon NJ, Park EY, Moon CS, Shin TJ, Yang TY, et al. Efficient, stable and scalable perovskite solar cells using poly(3-hexylthiophene). Nature 2019 Mar;567(7749):511–515. `https://www.nature.com/articles/s41586-019-1036-3`, number: 7749 Publisher: Nature Publishing Group.

[3] Green MA, Dunlop ED, Hohl-Ebinger J, Yoshita M, Kopidakis N, Ho-Baillie AWY. Solar cell efficiency tables (Version 55). Progress in Photovoltaics: Research and Applications 2020;28(1):3–15. `https://onlinelibrary.wiley.com/doi/abs/10.1002/pip.3228`, _eprint: https://onlinelibrary.wiley.com/doi/pdf/10.1002/pip.3228.

[4] Champion Photovoltaic Module Efficiency Chart | Photovoltaic Research | NREL;. `https://www.nrel.gov/pv/module-efficiency.html`.

[5] Rakocevic L, Mundt LE, Gehlhaar R, Merckx T, Aernouts T, Schubert MC, et al. Loss Analysis in Perovskite Photovoltaic Modules. Solar RRL 2019;3(12):1900338. `http://onlinelibrary.wiley.com/doi/abs/10.1002/solr.201900338`.

[6] Deng Y, Zheng X, Bai Y, Wang Q, Zhao J, Huang J. Surfactant-controlled ink drying enables high-speed deposition of perovskite films for efficient photovoltaic modules. Nature Energy 2018 Jul;3(7):560. `https://www.nature.com/articles/s41560-018-0153-9`.

[7] Japan's NEDO and Panasonic Achieve the World's Highest Conversion Efficiency of 16.09% for Largest-area Perovskite Solar Cell Module | Headquarters News;. `http://news.panasonic.com/global/press/data/2020/02/en200207-2/en200207-2.html`.

[8] Microquanta breaks efficiency record of large-area perovskite solar module;. `http://www.microquanta.com/en/newsinfo/C8C0D513B2569ECB/`.

[9] Di Giacomo F, Shanmugam S, Fledderus H, Bruijnaers BJ, Verhees WJH, Dorenkamper MS, et al. Up-scalable sheet-to-sheet production of high efficiency perovskite module and solar cells on 6-in. substrate using slot die coating. Solar Energy Materials and Solar Cells 2018 Jul;181:53–59. `http://www.sciencedirect.com/science/article/pii/S0927024817306190`.

[10] CEA, New record for Perovskite Module technology; 2020. `http://www.cea.fr/cea-tech/liten/en/Pages/News/2019/New-record-for-Perovskite-Module-technology.aspx`, library Catalog: liten.cea.fr Publisher: CEA.

[11] Abzieher T, Moghadamzadeh S, Schackmar F, Eggers H, Sutterlüti F, Farooq A, et al. Electron-Beam-Evaporated Nickel Oxide Hole Transport Layers for Perovskite-Based Photovoltaics. Advanced Energy Materials 2019;9(12):1802995. https://www.onlinelibrary.wiley.com/doi/abs/10.1002/aenm.201802995, _eprint: https://onlinelibrary.wiley.com/doi/pdf/10.1002/aenm.201802995.

[12] Li J, Wang H, Chin XY, Dewi HA, Vergeer K, Goh TW, et al. Highly Efficient Thermally Co-evaporated Perovskite Solar Cells and Mini-modules. Joule 2020 May;4(5):1035–1053. http://www.sciencedirect.com/science/article/pii/S2542435120300970.

[13] Rakocevic L, Gehlhaar R, Merckx T, Qiu W, Paetzold UW, Fledderus H, et al. Interconnection Optimization for Highly Efficient Perovskite Modules. IEEE Journal of Photovoltaics 2017 Jan;7(1):404–408.

[14] Qiu L, He S, Ono LK, Liu S, Qi Y. Scalable Fabrication of Metal Halide Perovskite Solar Cells and Modules. ACS Energy Letters 2019 Sep;4(9):2147–2167. https://doi.org/10.1021/acsenergylett.9b01396.

[15] Lee JW, Lee DK, Jeong DN, Park NG. Control of Crystal Growth toward Scalable Fabrication of Perovskite Solar Cells. Advanced Functional Materials 2019;29(47):1807047. http://onlinelibrary.wiley.com/doi/abs/10.1002/adfm.201807047.

[16] Palma AL. Laser-Processed Perovskite Solar Cells and Modules. Solar RRL;n/a(n/a):1900432. https://onlinelibrary.wiley.com/doi/abs/10.1002/solr.201900432.

[17] Haas S, Krumscheid S, Bauer A, Lambertz A, Rau U. Novel series connection concept for thin film solar modules. Progress in Photovoltaics: Research and Applications 2013;21(5):972–979. http://onlinelibrary.wiley.com/doi/abs/10.1002/pip.2188.

[18] Qiu W, Paetzold UW, Gehlhaar R, Smirnov V, Boyen HG, Tait JG, et al. An electron beam evaporated TiO2 layer for high efficiency planar perovskite solar cells on flexible polyethylene terephthalate substrates. Journal of Materials Chemistry A 2015 Nov;3(45):22824–22829. https://pubs.rsc.org/en/content/articlelanding/2015/ta/c5ta07515g, publisher: The Royal Society of Chemistry.

[19] Qiu W, Merckx T, Jaysankar M, Huerta CMdl, Rakocevic L, Zhang W, et al. Pinhole-free perovskite films for efficient solar modules. Energy & Environmental Science 2016 Feb;9(2):484–489. http://pubs.rsc.org/en/content/articlelanding/2016/ee/c5ee03703d.

[20] Rakocevic L, Ernst F, Yimga NT, Vashishtha S, Aernouts T, Heumueller T, et al. Reliable Performance Comparison of Perovskite Solar Cells Using Optimized Maximum Power Point Tracking. Solar RRL 2019;3(2):1800287. https://onlinelibrary.wiley.com/doi/abs/10.1002/solr.201800287.

[21] Krumscheid S, Optimizing the Interconnection Geometry of Thin-Film Solar Modules using the Finite Element Method. Juelich, Germany; 2010.

[22] Carver GP, Kopanski JJ, Novotny DB, Forman RA. Specific contact resistivity of metal-semiconductor contacts-a new, accurate method linked to spreading resistance. IEEE Transactions on Electron Devices 1988 Apr;35(4):489–497.

[23] IEK-5/SourceField;. https://github.com/IEK-5/SourceField.

[24] IEK-5, IEK-5/PVMOS; 2020. https://github.com/IEK-5/PVMOS, original-date: 2014-06-10T14:50:35Z.

[25] Kosasih FU, Rakocevic L, Aernouts T, Poortmans J, Ducati C. Electron Microscopy Characterization of P3 Lines and Laser Scribing-Induced Perovskite Decomposition in Perovskite Solar Modules. ACS Applied Materials & Interfaces 2019 Dec;11(49):45646–45655. https://doi.org/10.1021/acsami.9b15520.

[26] Barbé J, Newman M, Lilliu S, Kumar V, Lee HKH, Charbonneau C, et al. Localized effect of PbI2 excess in perovskite solar cells probed by high-resolution chemical–optoelectronic mapping. Journal of Materials Chemistry A 2018 Nov;6(45):23010–23018. http://pubs.rsc.org/en/content/articlelanding/2018/ta/c8ta09536a.

[27] Schultz C, Fenske M, Dagar J, Zeiser A, Bartelt A, Schlatmann R, et al. Ablation mechanisms of nanosecond and picosecond laser scribing for metal halide perovskite module interconnection – An experimental and numerical analysis. Solar Energy 2020 Mar;198:410–418. `http://www.sciencedirect.com/science/article/pii/S0038092X20300815`.

[28] Kim HS, Jang IH, Ahn N, Choi M, Guerrero A, Bisquert J, et al. Control of I–V Hysteresis in CH3NH3PbI3 Perovskite Solar Cell. The Journal of Physical Chemistry Letters 2015 Nov;6(22):4633–4639. `https://pubs.acs.org/doi/10.1021/acs.jpclett.5b02273`.

[29] Jeong J, Kang D, Chun DH, Shin D, Park JH, Cho SW, et al. Unveiling the origin of performance reduction in perovskite solar cells with TiO2 electron transport layer: Conduction band minimum mismatches and chemical interactions at buried interface. Applied Surface Science 2019 Nov;495:143490. `http://www.sciencedirect.com/science/article/pii/S0169433219322688`.

[30] Zhao X, Kim HS, Seo JY, Park NG. Effect of Selective Contacts on the Thermal Stability of Perovskite Solar Cells | ACS Applied Materials & Interfaces. ACS Applied Materials & Interfaces 2017;9(8):7148–7153. `https://pubs-acs-org.kuleuven.ezproxy.kuleuven.be/doi/10.1021/acsami.6b15673`.

GRAPHICAL ABSTRACT

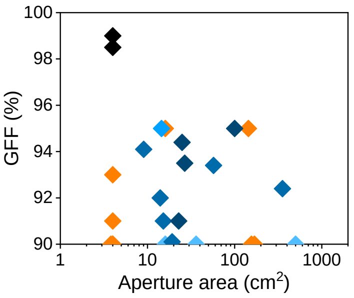

Cell-to-module upscaling loss of perovskite based thin-film photovoltaic technology is due to layer inhomogeneity loss and module design losses. We applied point contact interconnection design to decrease inactive area loss and achieve geometrical fill factor of up to 99 %. The graph shows in black results achieved in this study in comparison to other published perovskite modules. We characterize point contact interconnection using customized transfer line method and numerical simulations. Along with changes in cell-to-cell interconnection design, we analyze needed changes in the module design in order to achieve optimal balance between sheet resistance, contact resistance and inactive area loss.